Comprehensive modeling of hydrogen transport and accumulation in titanium and zirconium

AUTHOR(S):

Hamamoto, Yoshiki; Uchikoshi, Takeru; Tanabe, Katsuaki

CITATION:

Hamamoto, Yoshiki ...[et al]. Comprehensive modeling of hydrogen transport and accumulation in titanium and zirconium. Nuclear Materials and Energy 2020, 23: 100751.

ISSUE DATE:

2020-05

URL:

http://hdl.handle.net/2433/259428

Nuclear Materials and Energy 23 (2020) 100751

Contents lists available at ScienceDirect

Nuclear Materials and Energy

journal homepage: www.elsevier.com/locate/nme

Comprehensive modeling of hydrogen transport and accumulation in titanium and zirconium

Yoshiki Hamamoto, Takeru Uchikoshi, Katsuaki Tanabe*

Department of Chemical Engineering, Kyoto University, Nishikyo, Kyoto 615-8510, Japan

ARTICLE INFO

Keywords:
Metal
Hydride
Kinetic model
Adsorption
Absorption
Diffusion
Desorption
Hydrogen storage
Nuclear reactor
Fusion reactor

ABSTRACT

We developed kinetic models of hydrogen absorption in Ti and Zr. The models comprise series connections of the hydrogen-transport processes of surface dissociative adsorption and recombinative desorption; subsurface transport; and bulk diffusion. Numerical calculations using the models quantitatively reproduce the results of experimental series of time-transient absorption curves at various temperatures, demonstrating the validity of our models. Experimental desorption curves at various temperatures are also reproduced by the same model equations and kinetic parameters, particularly for Zr, demonstrating the dual functionality of our single model for hydrogen-transport directions. We use an effectiveness factor defined as the ratio between the real absorption rate and the virtual rate neglecting bulk diffusion. The transitions of the rate-determining steps of hydrogen transport in Ti and Zr under various conditions – such as temperature, pressure, and metal object size and shape – are systematically analyzed. As a case study to test the applicability of our model, hydrogen accumulation in the fuel claddings of light-water nuclear reactors was simulated to determine the cladding thickness required to prevent hydrogen embrittlement during the practical operation period. Our versatile kinetic models could be a useful tool that can aid the structural design and optimization of nuclear materials and facilities.

1. Introduction

Ti and Zr, and their hydrides, are important materials in applications such as hydrogen storage [1–5] and in nuclear reactor components [6–9]. Due to the importance of gaining an understanding of Ti and Zr hydrogenation processes, a number of studies have been conducted toward understand the kinetics in the hydrogen–Ti [10,11] and hydrogen–Zr [12–15] systems. Ti is used as a material for condenser tubes in nuclear reactors, owing to its high mechanical robustness and corrosion resistance against the sea water [6,16]. Due to its highly hydrogen-absorptive property, Ti is also used in sublimation pumps for hydrogen environments and for the long-term storage of tritium [11]. Zr is used in fuel claddings in light-water nuclear reactors for its high corrosion resistance as well as its low absorption cross-section for thermal neutrons which avoids slowing the fission reactions [17]. Ti and Zr alloys and hydrides are also promising for nuclear fusion applications, for example in reactors, as a coolant additives, and as radiation shielding [9,18,19]. Additionally, for hydrogen-storage applications, doping of Ti or Zr to low-surface-activity hydrogen-absorbing metals such as Mg can enhance the dissociative adsorption and recombinative desorption of hydrogen molecules [20].

Ti and Zr have some of the highest hydrogen-absorption capacities among metals [21]. The formation of Ti or Zr hydride through the absorption of hydrogen present in an operational environment causes problematic hydrogen embrittlement that can induce cracking and blistering of equipment [21]. There are three sources of hydrogen in nuclear reactors: (1) dissolved hydrogen existing in the cooling water or vapor, (2) radiation-induced decomposition of water, and (3) a chemical reaction between Zr and water ($Zr + 2H_2O \rightarrow ZrO_2 + 2H_2$) in the corrosion of Zr by water liquid or vapor [17]. Degradation by hydrogen embrittlement of the materials used in the construction of equipment can lead to fatal accidents such as the leakage of radioactive material or hydrogen detonation. Therefore, it is important to understand and consequently control hydrogen absorption into metallic components to prevent hydrogen embrittlement. The mechanism of hydrogen absorption in metals, however, has not been fully understood [22]. In the present study, we analyze the kinetics of hydrogen-absorption processes in Ti and Zr and develop hydrogen-transport models that are applicable to various shapes of metal parts at various temperatures.

* Corresponding author.
E-mail address: tanabe@cheme.kyoto-u.ac.jp (K. Tanabe).

https://doi.org/10.1016/j.nme.2020.100751
Received 11 March 2020; Received in revised form 20 April 2020; Accepted 28 April 2020
Available online 04 May 2020

2. Theory and calculation methods

2.1. Ti

The basic process of hydrogen absorption by metals proceeds as follows: First, gaseous hydrogen molecules dissociate into atoms at the metal surface, and then adsorb to surface sites. The hydrogen atoms migrate from the surface sites to subsurface sites, and eventually into the bulk where they diffuse. The region known as the subsurface is identified and defined in the literature [23–26], and is located at the transition region between the surface and the bulk of a material. The subsurface typically consists of one or two atomic monolayers lying immediately below the surface, and has a different chemical environment than either the surface or the bulk regions. Importantly, there is a difference in the activation energies for hydrogen absorption within the subsurface and bulk regions. For metals that have high surface activities for the dissociative adsorption of hydrogen molecules, such as Pd and Ti, the transport of hydrogen across the subsurface region often becomes the rate-determining step of hydrogen absorption. This lies in contrast to metals with lower surface activities, such as Mg and Zr. A significant discrepancy is frequently observed for the atomic coverage at the surface versus that at the subsurface – in high-surface-activity metals featuring low activation energies or low potential barriers – for the dissociative surface adsorption of hydrogen [24,25]. Therefore, hydrogen transport across the subsurface should be taken into account when developing numerical models intended to be used for highly accurate simulations of the net absorption rates of high-surface-activity metals. The earlier model for hydrogen absorption in Ti, proposed by Brown et al. [11], which did not account for the subsurface, had limitations such that it did not reproduce experimental data for the high-hydrogen-content regime. We have developed a versatile kinetic model of hydrogen absorption into Ti which accounts for the subsurface transport process. The basic concept of our model is schematically depicted in Fig. 1. We accounted for hydrogen fluxes related to the surface-adsorption and surface-desorption processes, subsurface transport between the surface and the bulk, and diffusion in the bulk region. The mass balances for the fractional coverages (occupancy) at the surface and subsurface (θ and θ_{ss}, respectively) and the hydrogen content X [mol-H/mol-Ti] can be expressed as follows:

$$N_s \frac{d\theta}{dt} = J_{ads} - J_{des} - J_{sb} + J_{bs} \tag{1}$$

$$N_s \frac{d\theta_{ss}}{dt} = J_{sb} - J_{bs} - J_{dif} \tag{2}$$

$$\frac{N_b V_b}{A} \frac{dX}{dt} = J_{sb} - J_{bs} \tag{3}$$

where J_{ads} and J_{des} are the hydrogen fluxes for the surface adsorption and desorption processes, respectively; J_{sb} and J_{bs} are the hydrogen fluxes for the inward and outward subsurface transport, respectively; J_{dif} is the hydrogen flux for the diffusion in the bulk region; N_s (2.16×10^{-5} mol·m^{-2}) is the number of atomic sites per unit of surface area of Ti; N_b (9.4×10^{4} mol·m^{-3}) is the number of atomic sites per unit of volume of Ti; V_b is the volume of Ti; and A is the surface area of Ti. N_s and N_b are determined by

$$N_s = \frac{(N_A N_b)^{\frac{2}{3}}}{N_A} \tag{4}$$

$$N_b = \frac{\rho}{M} \tag{5}$$

where N_A is the Avogadro constant, ρ is the mass density of Ti, and M is the molar mass of Ti. The J_{ads}, J_{des} [11], J_{sb}, J_{bs} [26], and J_{dif} values are calculated as follows:

$$J_{ads} = 2S_0(T)(1-\theta)^2 \frac{P_{H_2}}{\sqrt{2\pi M_{H_2} RT}} \tag{6}$$

$$J_{des} = {k_{des}}^0 \theta^2 \exp\left(-\frac{E_{des}}{RT}\right) \tag{7}$$

$$J_{sb} = {k_{sb}}^0 N_s \theta (1-\theta_{ss}) \exp\left(-\frac{E_{sb}}{RT}\right) \tag{8}$$

$$J_{bs} = {k_{bs}}^0 N_s \theta_{ss} (1-\theta) \exp\left(-\frac{E_{bs}}{RT}\right) \tag{9}$$

$$J_{dif} = {D_H}^0 \frac{\partial C(z,t)}{\partial z} \exp\left(-\frac{E_{dif}}{RT}\right) \tag{10}$$

where S_0 is the capturing coefficient; P_{H2} and M_{H2} are the partial pressure and molar mass of hydrogen, respectively; R and T are the ideal gas constant and the absolute temperature, respectively; ${k_{des}}^0$ (1.08×10^{8} mol·m^{-2} s^{-1} [11]), ${k_{sb}}^0$, and ${k_{bs}}^0$ are the frequency factors for the surface desorption, and the inward and outward subsurface transport of hydrogen atoms, respectively; E_{des} (1.17×10^{5} J·mol^{-1} [11]), E_{sb}, E_{bs}, and E_{dif} (5.3×10^{4} J·mol^{-1} [27]) are the activation energy values for the desorption, inward and outward subsurface transport, and diffusion of hydrogen in the bulk region, respectively; ${D_H}^0$ (9.0×10^{-7} m^2·s^{-1} [27]) is the pre-factor of the diffusion coefficient of hydrogen; and C is the local concentration of hydrogen in the bulk. Assuming that the adsorption to and desorption from the Ti surface are in equilibrium [11,28,29] owing to the high surface activity of Ti, from Eqs. (6) and (7), θ can be expressed as

$$\theta = \frac{\sqrt{\alpha}}{1+\sqrt{\alpha}} \tag{11}$$

where

$$\alpha = \frac{2S_0(T)P_{H_2}}{{k_{des}}^0 \exp\left(-\frac{E_{des}}{RT}\right)\sqrt{2\pi M_{H_2} RT}} \tag{12}$$

$S_0(T)$ is given by [11] as

$$S_0(T) = 0.0143 \exp\left(\frac{1.99\,[kJ/mol]}{RT}\right) \tag{13}$$

P_{H2} is determined via the ideal gas law as

$$P_{H_2} = \left\{\frac{P_0 V_{ch}}{RT} + \frac{(X_0 - X) n_{Ti}}{2}\right\} \frac{RT}{V_{ch}} \tag{14}$$

where P_0 is the initial hydrogen pressure, V_{ch}, is the chamber volume,

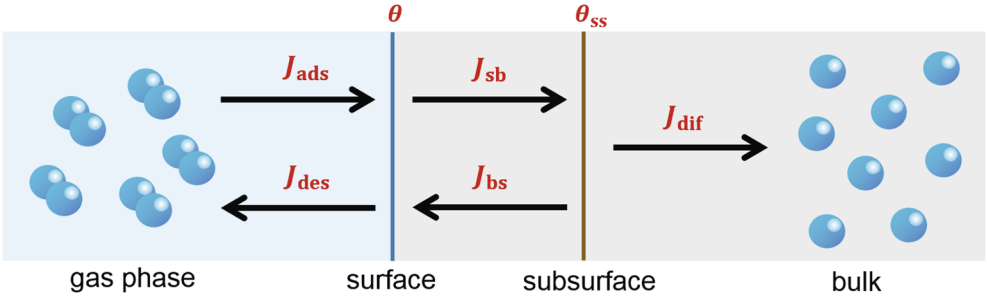

Fig. 1. Conceptual schematic diagram of our calculation model for hydrogen absorption into Ti. J_{ads} and J_{des} are the hydrogen fluxes for the surface adsorption and desorption processes, respectively; J_{sb} and J_{bs} are the fluxes for the migration of hydrogen from the surface to the subsurface, and from the subsurface to the surface, respectively; J_{dif} is the hydrogen flux for diffusion in the bulk region; and θ and θ_{ss} are the fractional coverages at the surface and subsurface, respectively.

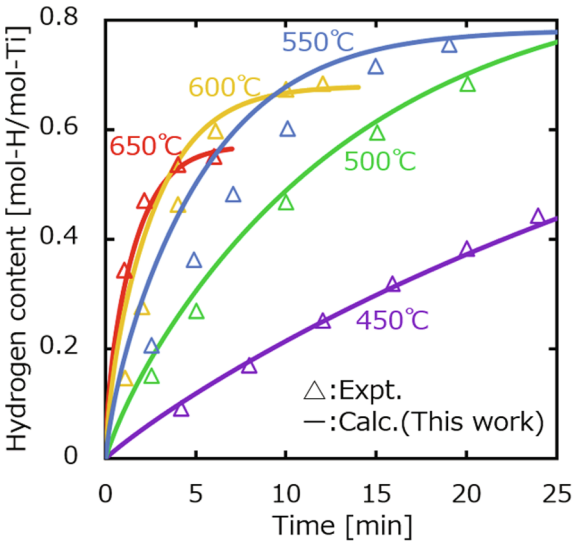

Fig. 2. Hydrogen-absorption curves for Ti at various temperatures (marks: experimental data [10], lines: calculation result). The fitting parameters were $k_{sb}{}^0 = 8.56 \times 10^{12}$ s^{-1}, $k_{bs}{}^0 = 7.77 \times 10^{13}$ s^{-1}, $E_{sb} = 1.36 \times 10^5$ J·mol^{-1}, and $E_{bs} = 1.60 \times 10^5$ J·mol^{-1} for all calculations.

X_0 is the initial hydrogen content in Ti, and n_{Ti} is the number of moles of Ti. Based on this model, we numerically solve the differential equations for one-dimensional transport using the finite-difference method to calculate the time evolution of the spatial hydrogen-concentration profile in Ti and thus X. For Ti plates, we apply the symmetric boundary condition or assume no flux of hydrogen on the central plane in Ti ($z = 0$), which is equivalent to simulating absorption from two opposite Ti surfaces. For Ti columns and spheres, we employ the axisymmetric and spherical symmetric coordinate systems [30], respectively. The Ti plates and columns are assumed to have infinite area and length, only accounting for the hydrogen transport in the directions of the plate thickness and column radius, respectively. We considered $k_{sb}{}^0$, $k_{bs}{}^0$, E_{sb}, and E_{bs} to be the fitting parameters for the transport of hydrogen atoms between the Ti surface and subsurface, and we determined them by using numerical fitting.

2.2. Zr

Subsurface transport seldom becomes rate-determining for hydrogen absorption or desorption in Zr owing to its low surface activity. This lies in contrast to the high-surface-activity metals such as Pd and Ti, which lead to a significant influence of the surface adsorption and desorption rates on the overall hydrogen-transport rate. For this reason, we did not account for the subsurface in our hydrogen-transport model for Zr. The mass balances for θ and X can be expressed as follows:

$$N_s \frac{d\theta}{dt} = J_{ads} - J_{des} - J_{dif} \tag{15}$$

$$\frac{N_b V_b}{A} \frac{dX}{dt} = J_{ads} - J_{des} \tag{16}$$

For Zr, from Eqs. (4) and (5), $N_s = 2.04 \times 10^{-5}$ mol·m^{-2} and $N_b = 7.15 \times 10^4$ mol·m^{-3}. The J_{ads}, J_{des}, and J_{dif} values can be calculated as follows:

$$J_{ads} = k_{ads}{}^0 (1-\theta) \frac{P_{H_2}}{\sqrt{2\pi M_{H_2} RT}} \exp\left(-\frac{E_{ads}}{RT}\right) \tag{17}$$

$$J_{des} = k_{des}{}^0 \theta \exp\left(-\frac{E_{des}}{RT}\right) \tag{18}$$

and Eq. (10) for J_{dif}. The variable $k_{ads}{}^0$ is the frequency factor for the surface adsorption of hydrogen atoms. Earlier hydrogen-absorption models for Zr comprised J_{ads} and J_{des} in the forms of zeroth- [15] and second- [13] order equations in terms of θ. Nevertheless, there has been no numerical model that can reproduce experimental data for the absorption and desorption processes from the low- to high-hydrogen-content region. In this study, we assumed a first-order dependence on θ for J_{ads} and J_{des}. As a reference, Fig. S1 shows an example of the fitting result of our model with a second-order dependence on θ for J_{ads} and J_{des} to the experimental hydrogen absorption curves of Ref. [12] for Zr at several temperatures. The reproducibility of the experimental data for the second-order case was observed lower than that for the first-order case to be presented in Section 3.2. From Ref. [12], we employed the values: $D_H{}^0 = 1.09 \times 10^{-7}$ m^2·s^{-1}, $E_{dif} = 4.77 \times 10^4$ J·mol^{-1}. We considered $k_{ads}{}^0$, $k_{des}{}^0$, E_{ads}, and E_{des} to be the fitting parameters, and determined them using numerical fitting.

3. Results and discussion

3.1. Ti

To demonstrate the validity of our kinetic model, we numerically produce results that match a set of experimental data for hydrogen absorption in Ti. Here we adopted the experimental values for hydrogen absorption into Ti plates, reported by Hirooka et al. [10], because it presents a series of time-evolution data for the hydrogen content in Ti at a variety of temperatures. Their experimental conditions were as follows: The size of the Ti plates was 1.0 cm × 1.3 cm × 1.0 mm. The initial pressure in the chamber, P_0, was 1.3×10^4 Pa. The chamber volume, V_{ch}, is not explicitly described in Ref. [10], so it was estimated to be 2.95×10^{-3} m^3 through the combination of Eq. (14) and

$$P_{\beta-eq}[atm] = \exp\left\{15.84 + 0.7X_{eq} + 2\ln\left(\frac{X_{eq}}{2 - X_{eq}}\right) - \frac{1.6 \times 10^4}{T[K]}\right\} \tag{19}$$

where $P_{\beta\text{-}eq}$ is the equilibrium pressure in the gas phase when Ti is in its β phase and X_{eq} is the equilibrium hydrogen content in Ti [31]. The combined equation was applied to the data at equilibrium for the β-phase region in Ref. [10]. Fig. 2 presents the fit of our model's calculation to the experimental hydrogen-absorption curves of Ref. [10] for Ti at several temperatures. We considered the kinetic parameters $k_{sb}{}^0$, $k_{bs}{}^0$, E_{sb}, and E_{bs} to be the numerical fitting parameters. We determined $k_{sb}{}^0$, $k_{bs}{}^0$, E_{sb}, and E_{bs} to be 8.56×10^{12} s^{-1}, 7.77×10^{13} s^{-1}, 1.36×10^5 J·mol^{-1}, and 1.60×10^5 J·mol^{-1}, respectively, for the transport of atomic hydrogen between the Ti surface and its subsurface. As can be observed in Fig. 2, we have demonstrated that the numerical calculations fit experimental data for a series of hydrogen absorption at different temperatures using a single set of material parameters. From another point of view, we have been able to finely extract the previously unknown kinetic parameters using the series of fittings. As a reference, the fitting result of our model, with the same single set of parameter values for $k_{ads}{}^0$, $k_{des}{}^0$, E_{ads}, and E_{des} as those for Fig. 2 for all calculations, to the experimental hydrogen desorption curves of Ref. [10] for Ti at several temperatures, is shown in Fig. S2. At higher temperatures, the experimental desorption curves are thus moderately reproduced by the same model equations and kinetic parameters for absorption, demonstrating the functionality of our single model for both hydrogen-transport directions.

After we obtained the kinetic parameters, we were able to perform simulations. Here, we analyzed the dependence of the hydrogen-absorption rate on a Ti piece's size and shape. Fig. 3 depicts numerical simulation results for the hydrogen-absorption curves for Ti plates of various thicknesses, under a hydrogen pressure of 1 atm at 600 °C. As the thickness of the Ti plates decreased, the hydrogen-absorption rate increased. This could be attributed to the smaller rate-determining effect by bulk diffusion in the thinner Ti plates owing to the sustainability of the hydrogen-concentration gradient. Fig. 4 depicts the numerically simulated hydrogen-absorption curves for a Ti plate, column, and

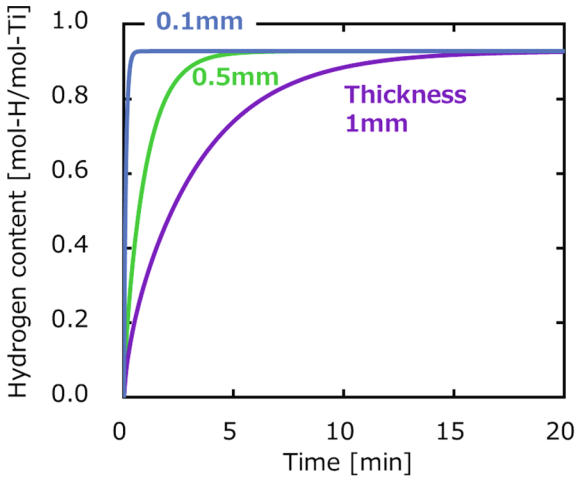

Fig. 3. Simulated hydrogen-absorption curves for Ti plates of various thicknesses under a hydrogen pressure of 1 atm at 600 ˚C.

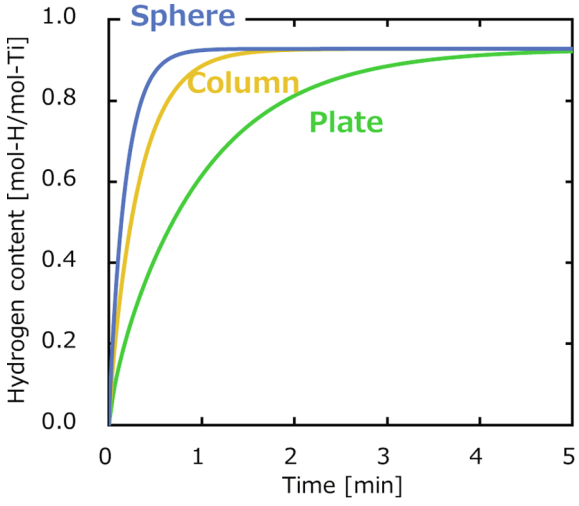

Fig. 4. Simulated hydrogen-absorption curves for a Ti plate, column, and sphere of a dimension (thickness or diameter) of 0.5 mm under a hydrogen pressure of 1 atm at 600 ˚C.

sphere with a size (thickness or diameter) of 0.5 mm under a hydrogen pressure of 1 atm at 600 ˚C. Among these different shapes of Ti, the hydrogen-absorption rate varied as follows: sphere > column > plate, for the same given dimension. The trend of this result is attributed to the difference in the specific surface area (surface area-to-volume ratio) among these different shapes. In addition, as can be observed in Figs. 3 and 4, we note that the equilibrium hydrogen contents of the objects are equal to one another, regardless of Ti sizes or shapes, because the equilibrium hydrogen content depends only on the hydrogen pressure and temperature.

Here we analyze the rate-determining steps of the overall hydrogen transport process. In Ref. [26], we defined the effectiveness factor, η, as the ratio of the actual hydrogen-absorption rate to the virtually calculated non-bulk-diffusion-controlled hydrogen-absorption rate. Numerically, η is calculated as $\eta = r_{obs}/r_{ideal}$, where r_{obs} and r_{ideal} are the actually observed hydrogen-absorption rate that accounts for bulk diffusion, and the virtual absorption rate that was calculated neglecting the bulk-diffusion process, which had been assumed to be much faster than the other processes. Concretely, each hydrogen-absorption rate is calculated as $r = dX/dt$. The factor η was specifically calculated in the high-hydrogen-content range, where η becomes constant [26]. For practical applications, the total hydrogen-absorption duration is mainly dominated by the duration of the absorption process in the high-

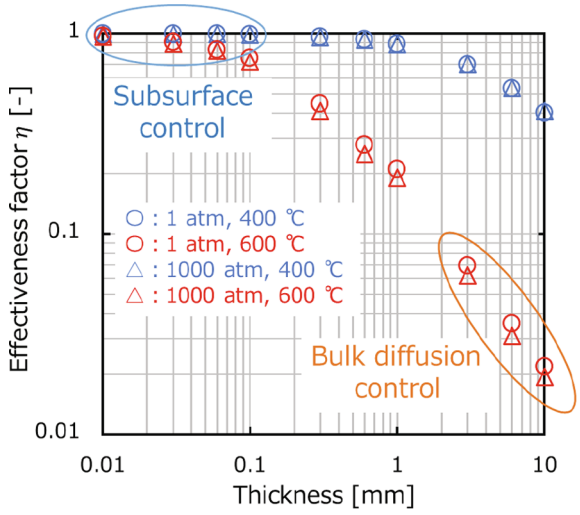

Fig. 5. Calculated η values for Ti plates of various thicknesses under hydrogen pressures of 1 and 1000 atm at 400 ˚C and 600 ˚C.

hydrogen-content range, where the absorption rate becomes lower and therefore the process requires more time. The factor η enables us to quantitatively evaluate the influence of each transport process and to determine the rate-determining step for different metal species and objects (e.g., sizes and shapes). Fig. 5 presents the calculated values of η for Ti plates of various thicknesses under hydrogen pressures of 1 and 1000 atm at 400 ˚C and 600 ˚C. The influence of the pressure increase on the change in η is small, which is attributed to the fact that the surface adsorption rate, which is strongly influenced by the hydrogen pressure, is sufficiently high relative to the bulk-diffusion rate, even under a hydrogen pressure of 1 atm. In contrast, the higher temperature is observed to significantly decrease η. This trend is explained as follows. From Eqs. (8) and (10), the increase in J_{sb} on temperature is larger than that for J_{dif}, due to E_{sb} being greater than E_{dif}. Therefore, the relative influence of bulk diffusion on the overall absorption rate increases at higher temperatures. The influence of bulk diffusion on the overall absorption rate also increases because the subsurface transport approaches equilibrium owing to the decreased J_{sb} and increased J_{bs}, which is due to the decreased θ at higher temperatures. In contrast, subsurface transport tends to be rate-determining at lower temperatures because E_{sb} is higher than E_{dif}, represented by larger η. There is a region of intermediate temperatures and thicknesses where one can neglect neither bulk-diffusion nor subsurface kinetics. Fig. 6 presents the calculated η values for Ti plates, columns, and spheres of various sizes (thicknesses or diameters) under 1 atm of hydrogen at 600 ˚C. For any shape made of Ti, η approaches unity, which corresponds to a state of subsurface transport control in the smaller size region; the enlargement of a Ti object shifts the state into one of bulk-diffusion control. This trend is attributed to the fact that the influence of bulk diffusion on the overall hydrogen-absorption rate decreases due to the decreased diffusion distance in the bulk for smaller Ti objects. It can be also observed from Fig. 6 that η increases in the order of plate < column < sphere, which is because spheres have smaller relative volumes and thus a smaller contribution of bulk diffusion that influence than do plates.

3.2. Zr

For Zr, we numerically reproduced, with our kinetic model, a set of experimental data for hydrogen absorption and desorption. We adopted the experimental data for hydrogen absorption and desorption in Zr plates by Gulbransen et al. [12] and Terrani et al. [15], respectively. For absorption [12], the dimensions of the Zr plate were 7.7 mm × 7.7 mm × 0.13 mm. The pressure in the chamber was kept constant at 6.7 × 10^3 Pa. The chamber volume was not described in

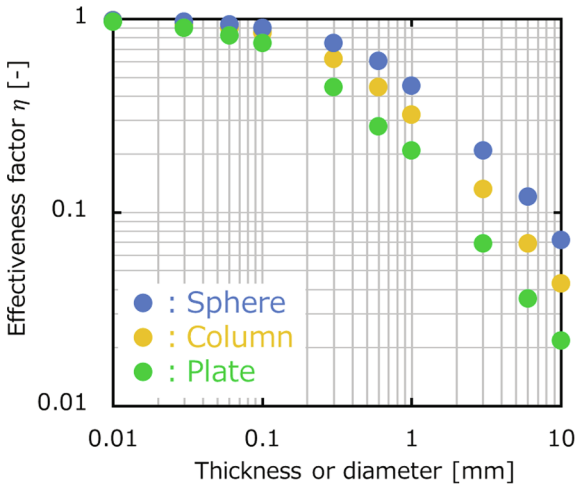

Fig. 6. Calculated η values for Ti plates, columns, and spheres of various dimensions (thicknesses or diameters) under a hydrogen pressure of 1 atm at 600 °C.

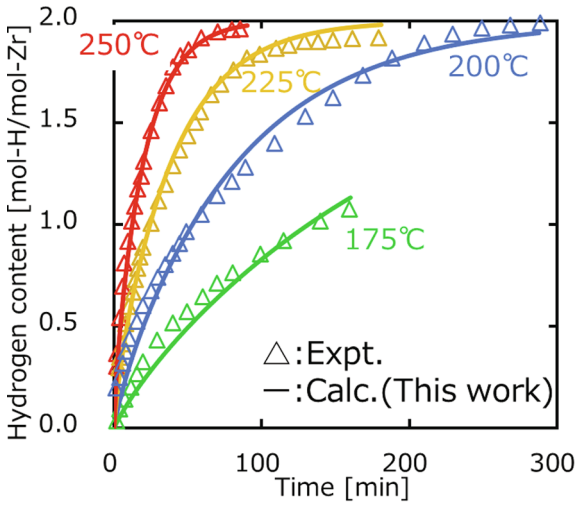

Fig. 7. Hydrogen-absorption curves for Zr at various temperatures (marks: experimental data [12], lines: calculation result). The fitting parameters were $k_{ads}{}^{0} = 9.62 \times 10^{2}\ s^{-1}$, $k_{des}{}^{0} = 3.00 \times 10^{7}\ s^{-1}$, $E_{ads} = 7.60 \times 10^{4}\ J{\cdot}mol^{-1}$, and $E_{des} = 1.14 \times 10^{5}\ J{\cdot}mol^{-1}$ for all calculations.

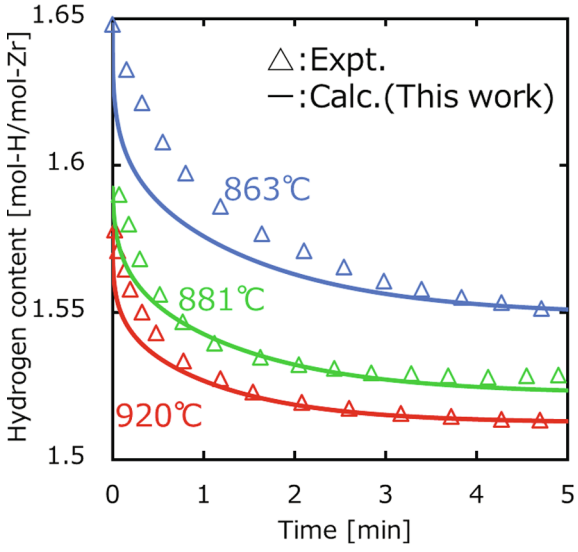

Fig. 8. Hydrogen-desorption curves for Zr at various temperatures (marks: experimental data [15], lines: calculation result). The same single set of parameter values for $k_{ads}{}^{0}$, $k_{des}{}^{0}$, E_{ads}, and E_{des} as those for Fig. 7 was used for all calculations.

Ref. [12], but this information is not necessary for numerical simulations owing to the constant hydrogen pressure. We used the reported experimental absorption curves for the temperatures of 175 °C, 200 °C, 225 °C, and 250 °C. The 150 °C data was considered anomalous and was not included, because the curves for 175, 200, 225, and 250 °C lined up at equal distances, while the curve for 150 °C unnaturally overlapped with the one for 175 °C. In addition, the 150 °C data had been recorded for only a truncated time range relative to the other temperatures, which was not sufficient for our numerical fitting. For desorption [15], the dimensions of the Zr circular plates were a diameter of 14 mm and a thickness of 1.04 mm. The initial pressure in the chamber was assumed to be 1.0×10^{-3} Pa. The chamber volume was $1.95 \times 10^{-5}\ m^{3}$. We employed the experimental desorption curves for the temperatures of 863 °C, 881 °C, and 920 °C out of the reported data. The other two temperatures were considered anomalous and were not included. For the 798 °C data, the given equilibrium pressure of 0.066 MPa and hydrogen content of 1.581 corresponds simply via the ideal gas law to a gas-phase pressure of 229 K, which was unrealistically low. For the 902 °C data, its hydrogen content unnaturally overlapped with that for 881 °C in the earlier time region and went even below that for 920 °C in the later time region, as observed in Fig. S3. Figs. 7 and 8 present the fitting results of our model to the experimental hydrogen absorption and desorption curves of Refs. [12,15], respectively, for Zr at several temperatures. For numerical fitting, we considered $k_{ads}{}^{0}$, $k_{des}{}^{0}$, E_{ads}, and E_{des} to be the fitting parameters. Through numerical fitting, we determined the kinetic parameters $k_{ads}{}^{0}$, $k_{des}{}^{0}$, E_{ads}, and E_{des} to be $9.62 \times 10^{2}\ s^{-1}$, $3.00 \times 10^{7}\ s^{-1}$, $7.60 \times 10^{4}\ J{\cdot}mol^{-1}$, and $1.14 \times 10^{5}\ J{\cdot}mol^{-1}$, respectively. The E_{ads} and E_{des} values that we obtained are similar to the experimentally determined values of $8.6 \times 10^{4}\ J{\cdot}mol^{-1}$ [15] and $1.13 \times 10^{5}\ J{\cdot}mol^{-1}$ [13], respectively. Importantly, as can be observed in Figs. 7 and 8, trends calculated by our model closely reproduced both the absorption and desorption experimental curves at various temperatures with a single set of kinetic parameters. There results validate our model for both hydrogen-transport directions, absorption and desorption.

Similarly to our analyses with Ti in the previous subsection, here we analyze the dependence of the hydrogen-absorption rate on the size and shape of Zr objects. Fig. 9 shows numerical simulation results for the hydrogen-absorption curves for Zr plates of various thicknesses under a hydrogen pressure of 1 atm at 200 °C. For the thinner Zr plates, the hydrogen-absorption rate increased. Again, this is attributed to the lesser influence of bulk diffusion for the thinner Zr plates, owing to the sustainability of the hydrogen concentration gradient. Fig. 10 depicts the numerically simulated hydrogen-absorption curves for a Zr plate, column, and sphere of 0.05 mm in size (thickness or diameter) and under a hydrogen pressure of 1 atm and a temperature of 200 °C. Among the different shapes, the hydrogen-absorption rate varied as follows: sphere > column > plate, for the same dimension, owing to the difference in specific surface area.

For the analysis of the rate-determining steps of the overall hydrogen-transport process for Zr, Fig. 11 shows the calculated η values for Zr plates of various thicknesses under hydrogen pressures of 1 and 10 atm and at 200 °C and 400 °C. Similar to the case of Ti, η was found to decrease when the temperature was increased. Nevertheless, in contrast to the case with Ti, η significantly decreases by the pressure increase from 1 to 10 atm. This large dependence of η on the hydrogen pressure is attributed to the fact that bulk diffusion becomes rate-determining as the surface adsorption and desorption processes approach equilibrium by the pressure increase because subsurface transport can be neglected for Zr. Fig. 12 shows the calculated η values for Zr plates, columns, and spheres of various sizes (thicknesses or diameters) under a

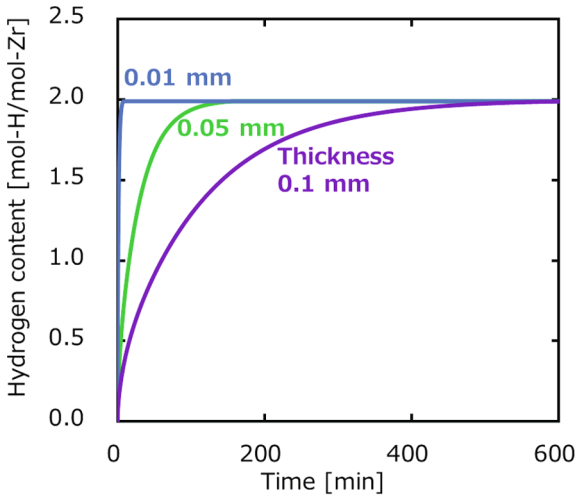

Fig. 9. Simulated hydrogen-absorption curves for Zr plates of various thicknesses under a hydrogen pressure of 1 atm at 200 °C.

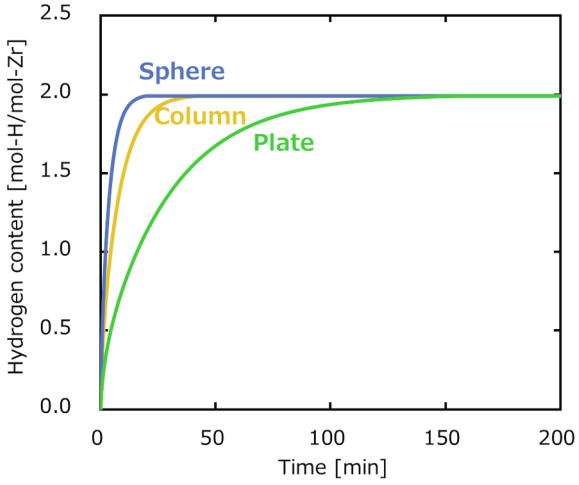

Fig. 10. Simulated hydrogen-absorption curves for a Zr plate, column, and sphere of a dimension (thickness or diameter) of 0.05 mm under a hydrogen pressure of 1 atm at 200 °C.

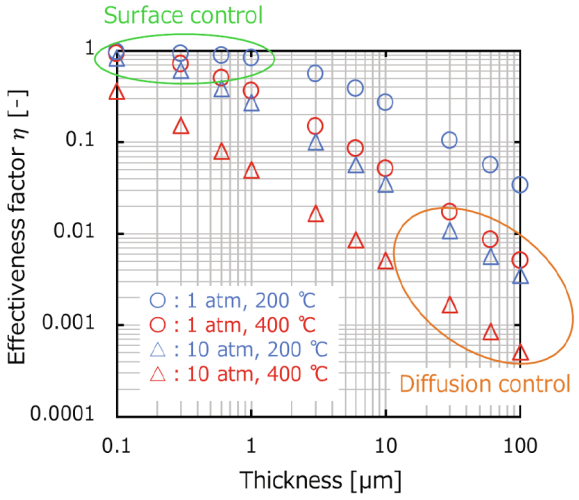

Fig. 11. Calculated η values for Zr plates of various thicknesses under hydrogen pressures of 1 and 10 atm at 200 °C and 400 °C.

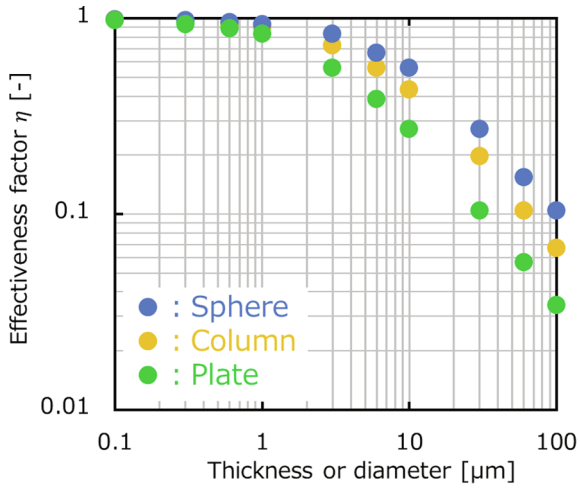

Fig. 12. Calculated η values for Zr plates, columns, and spheres of various dimensions (thicknesses or diameters) under a hydrogen pressure of 1 atm at 200 °C.

hydrogen pressure of 1 atm at 200 °C. For a Zr object of any shape, η approaches unity, which corresponds to the state of surface-adsorption/desorption control in the smaller size region, and for larger Zr objects turns the state into one of bulk-diffusion control. This tendency is attributed to the influence of the bulk diffusion on the overall hydrogen-absorption rate decreasing due to the shorter diffusion distance in the bulk for Zr objects of small sizes. It can also be observed in Fig. 12 that η increases in the order of plate < column < sphere, because spheres have smaller relative volumes for a given size, and thus a lesser bulk-diffusion influence than for plates, similar to the case of Ti.

3.3. Case study simulations

Herein we include a case study to demonstrate the usefulness of our numerical model. Using the hydrogen-absorption model for Zr, we investigated hydrogen transport and accumulation in nuclear fuel claddings. Zircaloy-2 and Zircaloy-4 are commonly used as cladding materials to cover the fuel rods in the pressurized chambers of nuclear reactors [32]. Zircaloys mainly consist of Zr, with mass fractions larger than 98%, and therefore we apply our model for Zr to the fuel claddings. In a reactor, fuel claddings are surrounded by cooling water or vapor, and the reaction between Zr and water generates hydrogen. Subsequent absorption of the hydrogen into the fuel cladding causes its hydrogen embrittlement.

First, we use our kinetic model to numerically reproduce the experimental data of hydrogen absorption in a nuclear fuel cladding reported by Cox et al. [33]. A number of the experimental conditions required for our numerical calculations are not described in Ref. [33]. Therefore, we employed common values for practical nuclear plants given in the literatures [34–37]. The outer diameter and thickness of the fuel cladding were 10.54 mm and 0.60 mm, respectively [37]. The temperature of the cooling water or vapor was 285 °C [34]. The temperature difference between the cooling water and the outer surface of the fuel cladding was 35 °C [35], and therefore the temperature of the outer surface of the fuel cladding was 320 °C. The spatial temperature slope in the interior of the fuel cladding, in the direction of the cladding radius, was 60 °C·mm^{-1} [36], and thus the temperature of the inner surface of the fuel cladding was 356 °C. The partial pressure of hydrogen was assumed to be 1.0×10^{-4} Pa, simply from the solubility product and molar volume of water. For the calculation, we treated the fuel cladding as an infinitely long circular tube, only accounting for the hydrogen transport in the direction of the tube radius. Fig. 13 presents the fitting result of our model calculation to the experimental hydrogen-absorption curve of Ref. [33]. Through numerical fitting, we

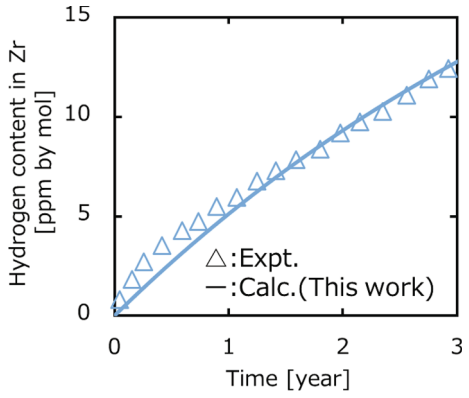

Fig. 13. Hydrogen-absorption curve for a nuclear fuel cladding (marks: experimental data, lines: calculation result). The fitting parameters were $k_{ads}{}^{0} = 9.62 \times 10^{2}\ s^{-1}$, $k_{des}{}^{0} = 3.00 \times 10^{7}\ s^{-1}$, $E_{ads} = 1.01 \times 10^{5}\ J{\cdot}mol^{-1}$, and $E_{des} = 1.53 \times 10^{5}\ J{\cdot}mol^{-1}$.

determined the kinetic parameters $k_{ads}{}^{0}$, $k_{des}{}^{0}$, E_{ads}, and E_{des} to be $9.62 \times 10^{2}\ s^{-1}$, $3.00 \times 10^{7}\ s^{-1}$, $1.01 \times 10^{5}\ J{\cdot}mol^{-1}$, and $1.53 \times 10^{5}\ J{\cdot}mol^{-1}$, respectively. These parameters are slightly different from those determined in the previous section for the Zr–gaseous-hydrogen system, presumably because the fuel cladding was surrounded by water molecules, which may increase E_{ads} and E_{des}. Another potential explanation is that ZrO_2 generated by the reaction between the fuel cladding and water covers the surface of the fuel cladding to form a stable oxide-layer barrier, which could also increase E_{ads} and E_{des}. We find that our hydrogen-absorption model is applicable to the metal–hydrogen systems in practical nuclear reactors.

Second, having obtained the kinetic parameters for hydrogen absorption in common fuel claddings, we performed simulations. Here, as a case study, we evaluated the thickness of fuel claddings on the basis of the operating conditions of a nuclear reactor. Fuel claddings are typically replaced and renewed every three years, simultaneously with the replacement of the fuel [38]. Accordingly, we determined the required thickness of the fuel cladding to satisfy the condition that the hydrogen content in the fuel cladding would not exceed 30 ppm, a concentration that would potentially cause severe hydrogen embrittlement [39], within three years. Fig. 14 presents the calculated dependence of the hydrogen content in the fuel cladding on the cladding thickness after three years. The required fuel-cladding thickness to prevent hydrogen embrittlement was found to be 0.25 mm, while the typical thicknesses

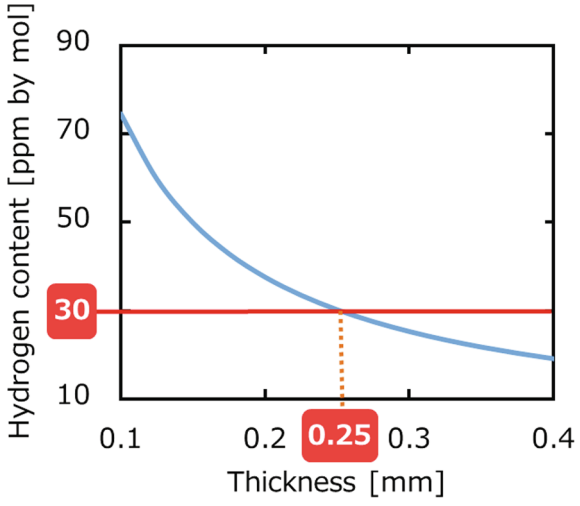

Fig. 14. Calculated dependence of the hydrogen content (in the fuel cladding) on the cladding thickness after three years of operational use in a nuclear reactor.

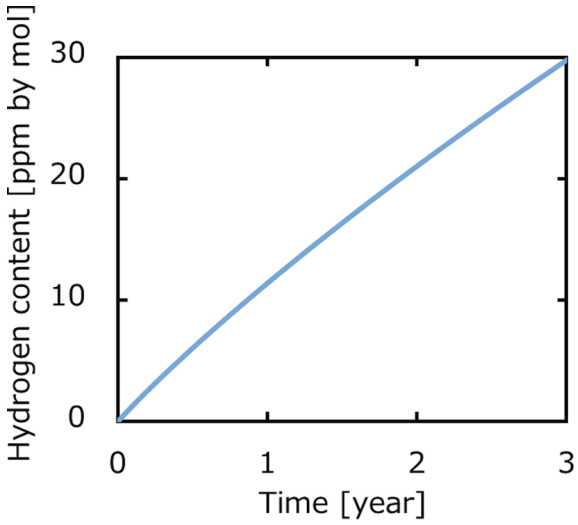

Fig. 15. Simulated hydrogen-absorption curve for a fuel cladding with a thickness of 0.25 mm.

of current practical fuel claddings are around 0.6–0.7 mm [37,40]. Fig. 15 depicts the numerically simulated hydrogen-absorption curve for a fuel cladding of 0.25 mm in thickness. In this manner, our kinetic model enables estimations, for example, of required cladding thicknesses for given conditions, such as fuel replacement frequencies, in view of hydrogen embrittlement.

4. Conclusions

In this study, we firstly developed a kinetic numerical model for hydrogen absorption in Ti accounting for the subsurface transport, which closely reproduces experimental data taken at various temperatures. We simulated the dependence of the hydrogen-absorption rate on the size and shape of Ti. For Zr, we developed a single model that reproduces experiments for both hydrogen absorption and desorption. We analyzed the influence of changes in the temperature and pressure on the transition of the rate-determining steps for hydrogen transport in Ti and Zr. Finally, as a case study, we demonstrated the applicability of our kinetic model. We evaluated the required thickness of fuel cladding in terms of hydrogen embrittlement according to the practical operating conditions of a nuclear reactor, such as the replacement frequency of fuel rods, by employing the model that we developed.

CRediT authorship contribution statement

Yoshiki Hamamoto: Methodology, Software, Validation, Formal analysis, Investigation, Data curation, Writing - original draft, Writing - review & editing, Visualization. **Takeru Uchikoshi:** Methodology, Software, Validation, Investigation, Writing - review & editing. **Katsuaki Tanabe:** Conceptualization, Methodology, Validation, Investigation, Resources, Writing - original draft, Writing - review & editing, Supervision, Project administration, Funding acquisition.

Declaration of Competing Interest

The authors declare that they have no known competing financial interests or personal relationships that could have appeared to influence the work reported in this paper.

Acknowledgements

This study was supported, in part, by the Japan Society for the Promotion of Science (JSPS).

Appendix A. Supplementary data

Supplementary data to this article can be found online at https://doi.org/10.1016/j.nme.2020.100751.

References

[1] R.M. Stroud, A.M. Viano, P.C. Gibbons, K.F. Kelton, S.T. Misture, Stable Ti-based quasicrystal offers prospect for improved hydrogen storage, Appl. Phys. Lett. 69 (1996) 2998–3000, https://doi.org/10.1063/1.117756.
[2] S.W. Cho, C.S. Han, C.N. Park, E. Akiba, Hydrogen storage characteristics of Ti-Zr-Cr-V alloys, J. Alloys Compd. 289 (1999) 244–250, https://doi.org/10.1016/S0925-8388(99)00162-0.
[3] C. Weidenthaler, A. Pommerin, M. Felderhoff, B. Bogdanovic, F. Schuth, On the state of the titanium and zirconium in Ti- or Zr-doped $NaAlH_4$ hydrogen storage material, Phys. Chem. Chem. Phys. 5 (2003) 5149–5153, https://doi.org/10.1039/b309409j.
[4] R. Kondo, S. Nakamichi, R. Azuma, Y. Takahashi, Y. Obora, H.T. Takeshita, Surface properties of air-exposed α-Ti-Pd alloys via XPS and cross-coupling reaction, Mater. Trans. 59 (2018) 1911–1914, https://doi.org/10.2320/matertrans.M2018240.
[5] S.E. Bambalaza, H.W. Langmi, R. Mokaya, N.M. Musyoka, J.W. Ren, L.E. Khotseng, Compaction of a zirconium metal-organic framework (UiO-66) for high density hydrogen storage applications, J. Mater. Chem. A 6 (2018) 23569–23577, https://doi.org/10.1039/c8ta09227c.
[6] M. Hedstroem, I. Multer, Titanium condenser – optimal solution for nuclear-power stations with seawater cooling, Trans. Am. Nucl. Soc. 31 (1979) 66–67.
[7] E.A. Marquis, J.M. Hyde, D.W. Saxey, S. Lozano-Perez, V. de Castro, D. Hudson, C.A. Williams, S. Humphry-Baker, G.D.W. Smith, Nuclear reactor materials at the atomic scale, Mater. Today 12 (2009) 30–37, https://doi.org/10.1016/S1369-7021(09)70296-2.
[8] T. Allen, J. Busby, M. Meyer, D. Petti, Materials challenges for nuclear systems, Mater. Today 13 (2010) 14–23, https://doi.org/10.1016/S1369-7021(10)70220-0.
[9] T. Tanaka, H. Muta, Y. Hishinuma, H. Tamura, T. Muroga, A. Sagara, Applicability of hydride materials for radiation shielding in helical reactor FFHR-D1, Fusion Sci. Technol. 68 (2015) 705–710 https://doi.org/10.13182/FST15-110.
[10] Y. Hirooka, M. Miyake, T. Sano, A study of hydrogen absorption and desorption by titanium, J. Nucl. Mater. 96 (1981) 227–232, https://doi.org/10.1016/0022-3115(81)90566-3.
[11] C.C. Brown, R.E. Buxbaum, Kinetics of hydrogen absorption in alpha titanium, Metall. Trans. A 19A (1988) 1425–1427, https://doi.org/10.1007/BF02674016.
[12] E.A. Gulbransen, K.F. Andrew, Diffusion of hydrogen and deuterium in high purity zirconium, J. Electrochem. Soc. 101 (11) (1954) 560, https://doi.org/10.1149/1.2781154.
[13] S. Naito, Kinetics of hydrogen absorption by α-zirconium, J. Chem. Phys. 79 (1983) 3113–3120, https://doi.org/10.1063/1.446142.
[14] K.A. Terrani, J.E. Seifried, D.R. Olander, Transient hydride fuel behavior in LWRs, J. Nucl. Mater. 392 (2009) 192–199, https://doi.org/10.1016/j.jnucmat.2009.03.010.
[15] K.A. Terrani, M. Balooch, D. Wongsawaeng, S. Jaiyen, D.R. Olander, The kinetics of hydrogen desorption from and adsorption on zirconium hydride, J. Nucl. Mater. 397 (2010) 61–68, https://doi.org/10.1016/j.jnucmat.2009.12.008.
[16] S. Anandan, R. Rajesh, K. Ganesh, A study of the condenser in nuclear power plants, Int. J. ChemTech Res. 10 (2017) 9–16 http://www.sphinxsai.com/2017/ch_vol10_no14/1/(09-16)V10N14CT.pdf.
[17] M. Steinbrück, Hydrogen absorption by zirconium alloys at high temperatures, J. Nucl. Mater. 334 (2004) 58–64, https://doi.org/10.1016/j.jnucmat.2004.05.007.
[18] C.B.A. Forty, P.J. Karditsas, Uses of zirconium alloys in fusion applications, J. Nucl. Mater. 283–287 (2000) 607–610, https://doi.org/10.1016/S0022-3115(00)00146-X.
[19] T. Hayashi, K. Tobita, Y. Nakamori, S. Orimo, J. Nucl. Mater. 386–388 (2009) 119–121, https://doi.org/10.1016/j.jnucmat.2008.12.073.
[20] M. Pozzo, D. Alfe, Hydrogen dissociation and diffusion on transition metal (= Ti, Zr, V, Fe, Ru Co, Rh, Ni, Pd, Cu, Ag)-doped Mg(0001) surfaces, Int. J. Hydrogen Energy 34 (2009) 1922–1930, https://doi.org/10.1016/j.ijhydene.2008.11.109.
[21] T.P. Chernyayeva, A.V. Ostapov, Hydrogen in zirconium part 1, Prob. Atomic Sci. Technol. 87 (2013) 16–31 https://pdfs.semanticscholar.org/41c9/b5a26c9bcff02c54fa05691614aaad4db0e6.pdf.
[22] K. Fukutani, M. Wilde, S. Ogura, Nuclear dynamics and electronic effects of hydrogen on solid surfaces, Chem. Rec. 17 (2017) 233–249, https://doi.org/10.1002/tcr.201600077.
[23] R.J. Behm, V. Penka, M.G. Cattania, K. Christmann, G. Ertl, Evidence for "subsurface" hydrogen on Pd(100): an intermediate between chemisorbed and dissolved species, J. Chem. Phys. 78 (1983) 7486–7490, https://doi.org/10.1063/1.444739.
[24] J. Greeley, M. Mavrikakis, Surface and subsurface hydrogen: adsorption properties on transition metals and near-surface alloys, J. Phys. Chem. B 109 (2005) 3460–3471, https://doi.org/10.1021/jp046540q.
[25] M. Wilde, K. Fukutani, Penetration mechanisms of surface-adsorbed hydrogen atoms into bulk metals: experiment and model, Phys. Rev. B 78 (2008) 115411, https://doi.org/10.1103/PhysRevB.78.115411.
[26] S. Ono, T. Uchikoshi, Y. Hayashi, Y. Kitagawa, G. Yeh, E. Yamaguchi, K. Tanabe, A heterothermic kinetic model of hydrogen absorption in metals with subsurface transport, Metals 9 (2019) 1131, https://doi.org/10.3390/met9101131.
[27] G.W. Wille, J.W. Davis, Hydrogen in titanium alloys, US DOE Technical Reports, 1981, DOE/ET/52039-2, doi: 10.2172/6420120.
[28] I. Ali-Khan, K.J. Dietz, F.G. Waelbroeck, P. Wienhold, The rate of hydrogen release out of clean metallic surfaces, J. Nucl. Mater. 76–77 (1978) 337–343, https://doi.org/10.1016/0022-3115(78)90167-8.
[29] T.L. Ward, T. Dao, Model of hydrogen permeation behavior in palladium membranes, J. Membr. Sci. 153 (1999) 211–231, https://doi.org/10.1016/S0376-7388(98)00256-7.
[30] Y. Kitagawa, K. Tanabe, Development of a kinetic model of hydrogen absorption and desorption in magnesium and analysis of the rate-determining step, Chem. Phys. Lett. 699 (2018) 132–138, https://doi.org/10.1016/j.cplett.2018.03.036.
[31] W.-E. Wang, Thermodynamic evaluation of the titanium-hydrogen system, J. Alloys Compd. 238 (1996) 6–12, https://doi.org/10.1016/0925-8388(96)02264-5.
[32] M.V. Glazoff, A. Tokuhiro, S.N. Rashkeev, P. Sabharwall, Oxidation and hydrogen uptake in zirconium, Zircaloy-2 and Zircaloy-4: computational thermodynamics and *ab initio* calculations, J. Nucl. Mater. 444 (2014) 65–75, https://doi.org/10.1016/j.jnucmat.2013.09.038.
[33] B. Cox, Effects of irradiation on the oxidation of zirconium alloys in high temperature aqueous environments: a review, J. Nucl. Mater. 28 (1968) 1–47, https://doi.org/10.1016/0022-3115(68)90055-X.
[34] R.W. Shumway, General features of emergency core cooling systems, Nucl. Power Safety (1976) 281–302, https://doi.org/10.1016/B978-0-08-021744-4.50014-2.
[35] J.C.A. Gaspar, M.L. Moreira, P.A.B. De Sampaio, Temperature distribution on fuel rods: a study on the effect of eccentricity in the position of UO2 pellets, in: Proc. 20th Int. Conf. Nucl. Energy New Europe, Bovec, Slovenia, 2011, pp. 814.1–814.11, https://www.nss.si/proc/nene2011/pdf/814.pdf.
[36] O. Courty, A.T. Motta, J.D. Hales, Modeling and simulation of hydrogen behavior in Zircaloy-4 fuel cladding, J. Nucl. Mater. 452 (2014) 311–320, https://doi.org/10.1016/j.jnucmat.2014.05.013.
[37] U. Ramasamy, L.F. Ibarra, R.A. Medina, Buckling behaviour of spent nuclear fuel rods, in: Proc. 23rd Int. Conf. Structural Mech. Reactor Technol., Manchester, UK, 2015, pp. 759.1–759.10, https://repository.lib.ncsu.edu/bitstream/handle/1840.20/34080/SMiRT-23_Paper_759.pdf.
[38] R.O. Abdel Rahman, R.Z. Rakhimov, N.R. Rakhimova, M.I. Ojovan, Cementitious Materials for Nuclear Waste Immobilization, Wiley, West Sussex, UK, 2014, , https://doi.org/10.1002/9781118511992.
[39] A. Griger, Z. Hozer, L. Matus, L. Vasaros, M. Horvath, Effect of hydrogen and oxygen content on the embrittlement of Zr alloys, in: Proc. IAEA Technical Committee Meeting, Halden, Norway, 2002, pp. 253–260, https://inis.iaea.org/collection/NCLCollectionStore/_Public/33/070/33070738.pdf.
[40] T.P. Chernyayeva, V.M. Grytsyna, V.S. Krasnorutskyy, A.P. Redkina, I.A. Petelguzov, Y.A. Slabospitskaya, Effects of Zr-1% Nb fuel rod cladding temperature and stressed conditions on hydridere orientation, Prob. Atomic Sci. Technol. 113 (2018) 189–202 https://vant.kipt.kharkov.ua/ARTICLE/VANT_2018_1/article_2018_1_189.pdf.